

# MauveSim: the instrument simulator software for the Mauve mission

Arianna Saba,<sup>1,2</sup>  Fabio Favata,<sup>1,3,4</sup> Giorgio Savini,<sup>1,2</sup> Giovanna Tinetti,<sup>1,2</sup> Lawrence Bradley,<sup>1</sup> Ian Stotessbury,<sup>1</sup> Marcell Tessenyi<sup>1</sup>

<sup>1</sup>Blue Skies Space Ltd., 69 Wilson Street, London, EC2A 2BB, UK

<sup>2</sup>Department of Physics and Astronomy, University College London, Gower Street, WC1E 6BT London, United Kingdom

<sup>3</sup>INAF - Osservatorio Astronomico di Palermo, Piazza del Parlamento, 1, 90134 Palermo, Italy

<sup>4</sup>Department of Physics, Imperial College London, Exhibition Road, London SW7 2AZ, United Kingdom

Accepted XXX. Received YYY; in original form ZZZ

## ABSTRACT

We present MauveSim, the instrument simulator software for Mauve, the latest mission from Blue Skies Space dedicated to time-domain stellar astronomy. The tool is designed to generate simulated stellar spectra, enabling the assessment of various scientific objectives, as well as determining limiting magnitudes and conducting signal-to-noise (S/N) analyses. MauveSim functions as an end-to-end simulator that takes an input stellar spectrum—either observed or synthetic—and produces a simulated observation based on the instrument’s performance and characteristics. The results of MauveSim have been validated against instrument performance data from extensive ground testing campaigns, ensuring that the software reflects the most up-to-date understanding of the payload performance. Accessible to all scientists involved in the mission, MauveSim serves as a crucial tool for target selection and observation planning.

**Key words:** time-domain stellar astronomy – simulator software – UV astronomy

## 1 INTRODUCTION

Born in the 1960s, mid and far ultraviolet (UV) astronomy coincided with the advent of space astronomy, as Earth’s atmosphere absorbs light at these wavelengths. Despite the great advancement of space astronomy in recent decades, UV observatories remain scarce and are often oversubscribed (e.g. the Hubble Space Telescope). In contrast, our understanding of astronomical objects and transient phenomena in the visible and near-infrared has expanded at an unprecedented pace driven by the large number of facilities deployed on the ground and in space. Time-domain astronomy, which focuses on the variable emission of sources, has been identified as a key priority for the next decade, as emphasised by the “Decadal Survey” outlining priorities for the USA research community (National Academies of Sciences Engineering, and Medicine 2021). A small space telescope capable of tracking variability across a broad wavelength range, including portions of the UV spectrum, will fill a crucial niche and enable unique scientific discoveries in this field (Egan et al. 2022; Indahl & Wilson 2022).

In this landscape, Blue Skies Space Ltd. (BSSL) has conceived Mauve, a UV mission designed to address the current gap in UV data availability. Mauve is a smallsat dedicated to time-domain spectrophotometry in the UV and Visible (UV-Vis) spectral range. Throughout its mission lifetime, Mauve will obtain time series of low-resolution spectra at  $\mathcal{R} = 20-65$  over a broad spectral range (200–700 nm), enabling the investigation of phenomena for which so far only fragmentary data have been collected.

Mauve’s design philosophy differs from traditional space science telescopes, which start from detailed science specifications around which a dedicated instrument is designed and built. While this approach results in high quality, high-performance instruments, it has traditionally come at significant financial cost. In keeping with BSSL’s philosophy (Archer et al. 2020), Mauve aims to fly commercial off-the-shelf (COTS) systems, resulting in a cost orders of magnitude lower than custom-designed instruments, albeit, unavoidably, with some performance compromises. In the case of Mauve, the key compromise is the high dark current from the detector due to the lack of a dedicated cryogenic system. Mauve is therefore optimised for long-term monitoring of the broad-band spectrophotometric variability of relatively bright sources, for which the high dark current is not a significant limiting factor.

In this paper, we present MauveSim, the instrument simulator developed by BSSL for the Mauve mission, incorporating information from design choices and instrument performance evaluated during multiple ground testing campaigns. An instrument simulator is a software tool that allows users to simulate how an astronomical instrument will see a given astronomical source and thus allows scientists to propose observations in an informed way. The instrument simulator encodes the best understanding of the instrument’s characteristics and performance. As such, it will naturally develop over time, as the understanding of the instrument evolves, and it will be updated in flight when the final calibration will be achieved. The tool is available to all scientists participating in the Mauve mission. We offer interested users outside of the mission the opportunity to access the software upon request.

\* E-mail: arianna@bssl.space (AS)

**Table 1.** Mauve's spectrometer and detector specifications.

Spectrometer Key Properties	
Grating	600 lines/mm
AD converter	16-bit, 6 MHz
Dimensions	105×80×20 mm
Weight	277.5 g
Detector Specifications	
Detector type	HAM S11639, CMOS linear array
Array Size	2048×1 pix
Pixel Size	14×200 $\mu\text{m}$
Read Noise	12 e <sup>-</sup> rms
Dark current	445 counts/pix · s (at 21°C)

## 2 PAYLOAD COMPONENTS

The Mauve payload consists of three main components: a telescope, an optical fibre and a spectrometer. The payload has been designed with redundancy in mind, so the current baseline includes the provision of two fibre+spectrometer units to cope with a potential failure of the primary unit. The telescope and optical components are housed separately from the spacecraft platform equipment to minimise thermal variations throughout the orbit and reduce thermo-elastic distortions. The design, being developed by C3S and ISISpace, leverages heritage components where feasible and utilises the product lines and supply chains of both companies ([Stotesbury et al. in prep.](#)).

The selected telescope is a Cassegrain telescope of 13 cm aperture originally designed for space-based optical communications by MediaLario, Italy. The telescope has already undergone a wide range of optical, thermal and vibration tests as part of qualification campaigns on other satellites and required only two minor modifications to be compatible with the Mauve satellite:

- As the telescope was originally designed for laser optical communication, the standard coating is optimised for 1550 nm. The current anti-reflection (AR) coating has been replaced with a coating designed to improve the signal in the UV range.
- To mount the fibre between the telescope and the spectrometer, MediaLario modified the mount of the telescope in order for the fibre to be placed at the telescope focus. The fibre will exit from the back of the primary mirror and connect to the spectrometer, aligning its output with the spectrometer aperture.

The spectrometer is produced by Avantes, Netherlands. The unit is a high-quality, COTS spectrometer used across biomedicine, semiconductor coating detection and other terrestrial applications. The spectrometer houses a diffraction grating, a detector collection lens (DCL), and a window to limit contamination into the spectrometer through the connector port. The spectrometer operates from 200 to 700 nm across a single channel, illuminating a CMOS line array detector from Hamamatsu ([HAMAMATSU 2024](#)). Spectrometer and detector characteristics are given in Table 1.

## 3 INSTRUMENT PERFORMANCE

To evaluate Mauve's scientific performance, we used real measurements of the telescope, fibre, and spectrometer obtained during multiple test campaigns at MediaLario. Performance was measured in the visible spectrum (using a 636 nm filter) and in the UV wavelengths (using a 248 nm filter). The payload performance is primarily influenced by two key factors: the light throughput across the system

**Table 2.** Instrument performance specifications.

Parameter	Value
Detector temperature	21°C
Dark current	445 counts/s
System's optical efficiency	66%

and the detector's dark current, which increases exponentially with temperature.

Regarding the first point, recent integrated payload tests revealed an overall optical efficiency of 66% throughout the system.

As for the second point, the thermal model provided by the suppliers assumes a detector operating temperature of 21°C. While dedicated spacecraft instruments typically operate at cooler temperatures, Mauve's COTS spectrograph is subject to higher temperatures due to design constraints. Ongoing work with the manufacturing partners aims to lower the detector temperature to a target of 13°C. A refined thermal analysis, including a margin approach, suggests that this could halve the dark current and significantly improve instrument performance.

The example science simulations in Sec. 5 are based on conservative assumptions regarding the detector temperature and the system's optical efficiency measured in the lab as presented in Table 2.

A third factor influencing and potentially limiting scientific performance is relying on payload data for pointing, rather than solely using star tracker information. This approach will be essential to compensate for the expected thermal distortion caused by the spacecraft crossing the Earth's terminator during each orbit. Our concept consists in determining the fraction of time that the source's light is actually collected by the fibre, as opposed to being lost when the source falls outside the fibre. The approach taken in defining the diameter of the fibre and thus the Field of View (FoV) has been to use the high-frequency pointing performance of the spacecraft. This has been modelled by ISISpace using the Moments of Inertia (MoI) calculations of the mature mechanical model and the ADCS controller and actuators in the system. The analysis has produced a Power Spectral Density (PSD) which predicts a high-frequency pointing stability of approximately 12" (10 s rms). We then used this information to conduct a time-domain analysis of the jitter, which helped us determine the fibre width. We selected a fibre diameter of 230  $\mu\text{m}$ , corresponding to a half-cone FoV of approximately 47". The algorithm developed by BSSL to correct for low-frequency pointing distortions is called "Payload In The Loop" (PITL) and it will be described in [Bradley et al. \(in prep.\)](#). However, the instrument simulator does not rely on the performance of the PITL and the results shown here assume that the spacecraft can lock onto and follow the target source selected for the simulation.

## 4 WORKFLOW STRUCTURE

MauveSim produces synthetic Mauve observations by applying a series of steps. These can be grouped in 4 broad categories.

- *Preparing the input spectrum:* Downsampling the initial number of data points, scaling the visible magnitude of the target source, including zodiacal background contamination.
- *Convolving the spectrum to the resolution of the instrument:* Applying the instrument line function (ILF) to match the input data to the spectral resolution of the spectrometer.
- *Converting flux into counts:* Considering the efficiencies of

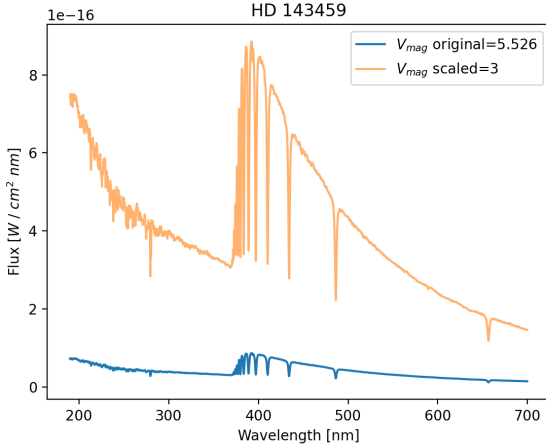


Figure 1. Magnitude comparison for the star HD 143459.

the payload components, the telescope aperture, detector quantum efficiency, wavelength coverage per pixel, exposure time and conversion factors.

(iv) *Adding astrophysical and instrumental noise sources*: Including photon noise, dark current and bias.

#### 4.1 Preparing the input spectrum

The simulator takes as input a source spectrum in the Mauve wavelength range (200-700 nm) expressed as a list of wavelengths paired with corresponding fluxes. The input spectrum can be either synthetic or the result of observations with other instruments. Stellar model SEDs, e.g. ATLAS9 models from Castelli & Kurucz<sup>1</sup> can be used to simulate Mauve observations, as long as they are provided in the format requested by the software. Alternatively, one can employ databases of observed stellar spectra. An example is the HST/STIS Low-resolution Stellar Library<sup>2</sup> (Pal et al. 2023) which provides more than 500 calibrated stellar spectra across the 200-1000 nm wavelength region at  $\mathcal{R} \sim 1000$ . Spectra from the STIS library are given in units of Å for the wavelength and  $\text{erg s}^{-1} \text{cm}^{-2} \text{Å}^{-1}$  for the flux. The flux is provided with an uncertainty as well.

Once the user selects the input spectrum, this is downsampled if it contains more than 2048 data points. This interpolation is necessary to ensure that each wavelength data point is consistent with the association of the detector array with the range created by the combination of the grating plus order sorting filter.

The star taken as an example here, HD 143459, has a V magnitude of 5.526. To simulate the same spectrum but with a different magnitude, the flux needs to be scaled according to

$$F = F_0 \cdot 10^{-\Delta m/2.5}, \quad (1)$$

where  $F_0$  is the original flux and  $\Delta m = m_{\text{final}} - m_{\text{initial}}$ , i.e. the difference between the final wanted magnitude (e.g.  $V_{\text{mag}} = 3$ ) and the initial magnitude (in this case  $V_{\text{mag}} = 5.526$ ). Fig. 1 displays the original spectrum of HD 143459 retrieved from the STIS stellar database, alongside its version scaled to a visual magnitude of 3.

The flux is then converted from units of  $\text{erg s}^{-1} \text{cm}^{-2} \text{Å}^{-1}$  to

Helio-ecliptic Longitude (deg)	Helio-ecliptic Latitude (deg)						
	0°	15°	30°	45°	60°	75°	90°
180°	22.1	22.4	22.7	23.0	23.2	23.4	23.3
165°	22.3	22.5	22.8	23.0	23.2	23.4	23.3
150°	22.4	22.6	22.9	23.1	23.3	23.4	23.3
135°	22.4	22.6	22.9	23.2	23.3	23.4	23.3
120°	22.4	22.6	22.9	23.2	23.3	23.3	23.3
105°	22.2	22.5	22.9	23.1	23.3	23.3	23.3
90°	22.0	22.3	22.7	23.0	23.2	23.3	23.3
75°	21.7	22.2	22.6	22.9	23.1	23.2	23.3
60°	21.3	21.9	22.4	22.7	23.0	23.2	23.3
45°	SA	SA	22.1	22.5	22.9	23.1	23.3
30°	SA	SA	SA	22.3	22.7	23.1	23.3
15°	SA	SA	SA	SA	22.6	23.0	23.3
0°	SA	SA	SA	SA	22.6	23.0	23.3

Figure 2. Zodiacal sky background ( $V_{\text{mag}} \text{ arcsec}^{-2}$ ) as a function of helio-ecliptic coordinates. Table from [COS Instrument Handbook](#).

$\text{W cm}^{-2} \text{nm}^{-1}$  to match the units of the quantities used to convert the flux to counts, e.g. the detector quantum efficiency (QE) which is given in units of A/W.

To calculate the zodiacal noise, we use a table of approximate zodiacal sky background as a function of helio-ecliptic coordinates. First, the user is prompted to provide the RA, Dec and time of observation (UTC) to check if the target is within the observing zone or in the solar-avoidance zone. The equatorial coordinates RA and Dec are first converted to geocentric ecliptic coordinates using `astropy` modules. In the geo-ecliptic coordinate system, the zero longitude is defined by the vernal equinox. However, the zodiacal light is a function of the Sun's position. This is what defines the zero longitude in the helio-ecliptic coordinate system. Thus, by using the input time of observation, the Sun's position from Earth's perspective is calculated at the given time. Then, the Sun's position is transformed to geocentric ecliptic coordinates (Leinert et al. 1998). The geocentric ecliptic coordinates are converted to helio-ecliptic coordinates according to:

$$\begin{aligned} \lambda_{\text{helio}} &= \lambda_{\text{geo}} - \lambda_{\odot}, \\ \beta_{\text{helio}} &= \beta_{\text{geo}}, \end{aligned} \quad (2)$$

where  $\lambda$  represents longitude,  $\beta$  represents latitude and  $\lambda_{\odot}$  represents the Sun geo-ecliptic longitude. Therefore, the level of zodiacal light is a function of the position of the star in the sky and of the time it is observed (more or less close to the Sun). The helio-ecliptic coordinates thus defined are then assigned the corresponding level of zodiacal background, using the reference table in Fig. 2.

The zodiacal sky background is given in units of  $V_{\text{mag}} \text{ arcsec}^{-2}$ . To convert it into flux, we follow the steps below. Assuming that the zodiacal background has a signature similar to the Solar spectrum, we take the spectrum of HD 126614 (a G8 star) and scale its magnitude to

$$V_{\text{total}} = V_{\text{zodi}} - 2.5 \log_{10}(A_{\text{FoV}}). \quad (3)$$

$V_{\text{total}}$  is calculated by taking into account the magnitude of the zodiacal light read off from the table ( $V_{\text{zodi}}$ ) and the field of view of the telescope ( $A_{\text{FoV}}$ ), which is 47.46 arcsec in diameter, 1769 arcsec<sup>2</sup> in area. Equation 3 comes from the relationship between surface bright-

<sup>1</sup> <https://wwwuser.oats.inaf.it/fiorella.castelli/>

<sup>2</sup> <http://astro.wsu.edu/hststarlib/>

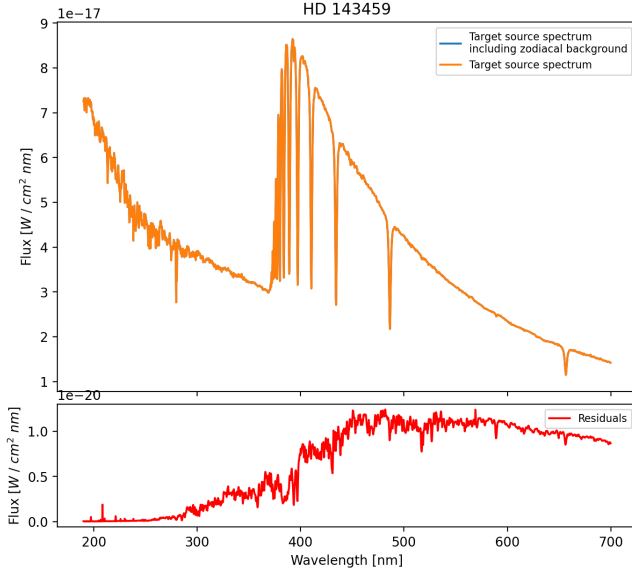


**Figure 3.** Target stellar spectrum with and without the inclusion of zodiacal background. While the spectra are indistinguishable, the residuals reveal a solar-type spectrum characteristic of zodiacal light.

ness (magnitude per square arcsecond) and the total magnitude over a given area. The surface brightness ( $V_{\text{zodi}}$ ) is the apparent magnitude per square arcsecond. It describes how bright an object appears spread over one square arcsecond of the sky. The total magnitude ( $V_{\text{total}}$ ) is the total apparent magnitude of an object when considering the entire area it covers. When a surface brightness is given in square arcseconds, it is necessary to account for how the flux adds up over that area. The total flux is the surface brightness flux multiplied by the area:

$$F_{\text{total}} = F_{\text{zodi}} \times A_{\text{FoV}} \quad (4)$$

To convert flux to magnitude, we employ the usual relationship:

$$m_1 - m_2 = -2.5 \log_{10} \left( \frac{F_1}{F_2} \right), \quad (5)$$

where  $m_1 = V_{\text{total}}$ ,  $m_2 = V_{\text{zodi}}$ ,  $F_1 = F_{\text{total}}$ , and  $F_2 = F_{\text{zodi}}$ , such that

$$V_{\text{total}} - V_{\text{zodi}} = -2.5 \log_{10} \left( \frac{F_{\text{total}}}{F_{\text{zodi}}} \right). \quad (6)$$

Since  $F_{\text{total}} = F_{\text{zodi}} \times A_{\text{FoV}}$ , then

$$V_{\text{total}} - V_{\text{zodi}} = -2.5 \log_{10}(A_{\text{FoV}}). \quad (7)$$

If the spectrum has a coverage beyond 200–700 nm, the software considers only the wavelengths between 200 and 700 nm.

Fig. 3 illustrates how the target spectrum is altered by the inclusion of the zodiacal background. While the two spectra appear visually indistinguishable, the residuals reveal that the difference corresponds to a solar-type spectrum with an average  $V_{\text{mag}} = 22$ .

## 4.2 Calculating the source signal

To express the spectrum according to the resolution of the instrument, MauveSim convolves the result of step 4.1 with a kernel that downgrades the data to the resolution achievable by Mauve. Here we

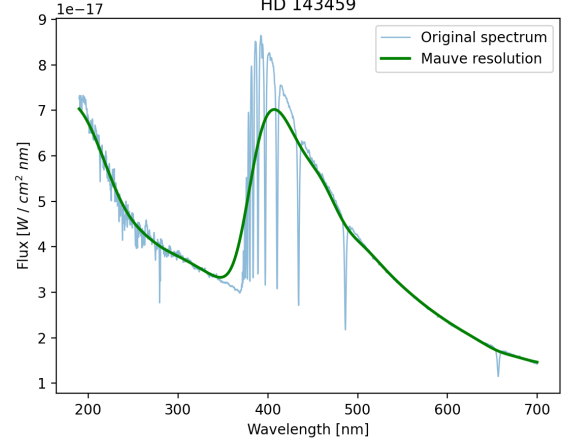


**Figure 4.** The spectrum of HD 143459, obtained using HST/STIS, has been convolved to Mauve's resolution using a combination of Gaussian and top-hat kernels. The graph illustrates a resolution comparison. However, it is important to note that the spectrum in green does not represent the flux levels achievable by Mauve.

convolve the stellar spectrum with a kernel (a smoothing function), that is defined by the instrument line function (ILF).

The convolution  $y(\lambda)$  of a spectrum  $x(\lambda)$  with a kernel  $k(\lambda)$  is given by:

$$y(\lambda) = (x * k)(\lambda) = \int_0^\infty x(\lambda') k(\lambda - \lambda') d\lambda'. \quad (8)$$

Here,  $y(\lambda)$  is the resulting convolved spectrum,  $x(\lambda)$  is the stellar spectrum,  $k(\lambda)$  is the kernel function, and  $\lambda$  represents the wavelength.

The instrument line function, determines how the original spectral data gets broadened. The Mauve ILF features two components: a “top hat” element due to the fibre and a Gaussian component due to the spectrograph. A one-dimensional top hat kernel centred at  $\lambda = 0$  with width  $2a$  (i.e., it extends from  $-a$  to  $a$ ) is defined as:

$$k(\lambda) = \begin{cases} \frac{1}{2a} & \text{if } |\lambda| \leq a \\ 0 & \text{if } |\lambda| > a \end{cases} \quad (9)$$

Here,  $k(\lambda)$  is the kernel function, and  $a$  is a positive constant representing half the width of the kernel. The kernel is normalised so that the total area under the curve is 1:

$$\int_0^\infty k(\lambda) d\lambda = 1. \quad (10)$$

According to the spectrometer specifications, for a grating of 600 lines/mm and a  $500 \mu\text{m}$  slit, the resolution is  $108 \text{ \AA}$ . This is the width of the boxcar kernel.

The Gaussian kernel is defined by its characteristic bell-shaped curve

$$k(\lambda) = \frac{1}{\sigma \sqrt{2\pi}} e^{-\frac{\lambda^2}{2\sigma^2}}. \quad (11)$$

The standard deviation  $\sigma$  determines the width of the kernel, which directly influences the degree of resolution reduction. A broader kernel, corresponding to a larger  $\sigma$ , results in a more pronounced smoothing effect, leading to a greater reduction in resolution.

Mauve has constant resolution with wavelength, meaning that the value of  $\Delta\lambda$ , the smallest resolvable wavelength difference, is the

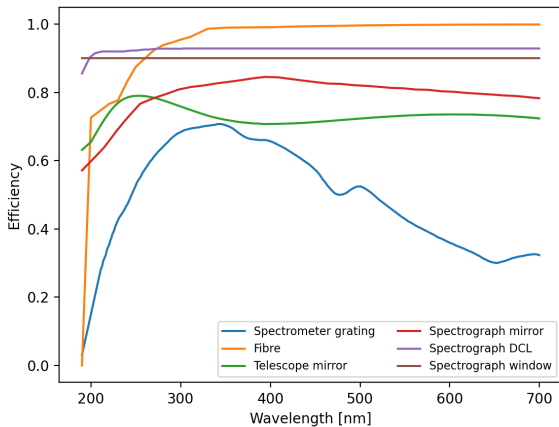


**Figure 5.** Efficiencies of the Mauve payload components.

same throughout the entire wavelength range of the instrument. For Mauve,  $\Delta\lambda \approx 105 \text{ \AA}$ , which determines the FWHM of the Gaussian kernel. The top hat kernel and Gaussian kernel are first convolved together, then their convolution is applied to the data. The convolution order does not matter as it is a commutative operation. Fig. 4 displays the resolution achievable by Mauve.

#### 4.3 Converting flux into counts

The stellar spectrum convolved at the resolution of Mauve is converted from flux to counts, in units of digital numbers (DN). First, the various payload efficiencies are considered, as illustrated in Fig. 5. These include:

- grating efficiency ( $GR$ ),
- fibre efficiency ( $FB$ ),
- coupling losses ( $CL$ ),
- two telescope mirrors ( $MT$ ),
- two spectrograph mirrors ( $MS$ ),
- spectrometer DCL efficiency ( $DCL$ ),
- spectrometer window efficiency ( $WD$ ),
- system's optical efficiency ( $OE$ ).

The overall instrumental efficiency is determined by multiplying these factors together:

$$\text{efficiency} = GR \cdot FB \cdot (1 - CL)^4 \cdot MT^2 \cdot MS^2 \cdot DCL \cdot WD \cdot OE. \quad (12)$$

The coupling loss is currently defined as a 4% loss at each fibre connection and at each boundary of the spectrometer window. The instrumental efficiency is then combined with the detector quantum efficiency ( $QE$ ), expressed in units of A/W, to determine the system's overall throughput. Both the quantum efficiency and the resulting throughput are illustrated in Fig. 6.

We combine the result thus obtained with the telescope's collecting area,  $A$ , the wavelength range per pixel,  $\Delta\lambda_\lambda$ , and the exposure time,  $t_{\text{exp}}$ . During the testing campaign, Mauve's primary aperture was measured to be  $122 \text{ cm}^2$ . The wavelength range per pixel,  $\Delta\lambda_\lambda$ , was found to vary between 0.25 and 0.30 nm across the 2048 pixels that constitute the detector. The exposure time,  $t_{\text{exp}}$ , represents the duration of the observation. Extended exposure times improve the signal-to-noise ratio (S/N), as the signal increases linearly while photon noise grows more slowly, scaling with the square root of the

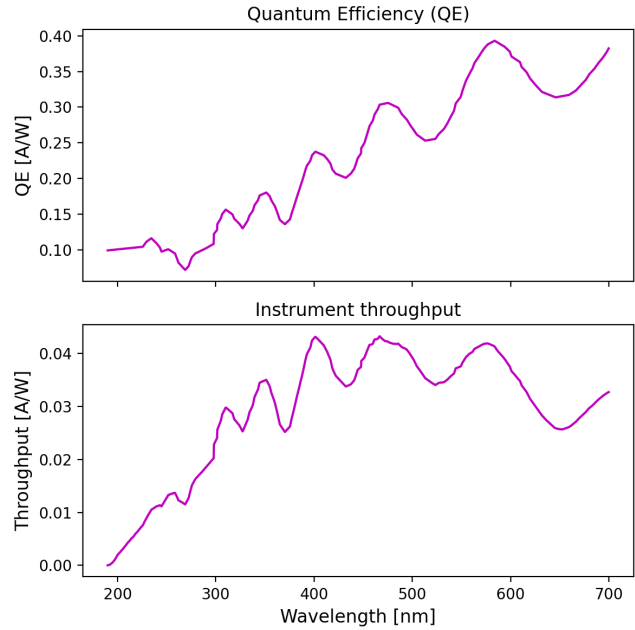


**Figure 6.** Upper panel: Mauve's detector quantum efficiency. Lower panel: Instrumental throughput, calculated as the product of the detector QE and the total instrumental efficiency defined in Eq. 12.

exposure time. The input flux (in units of  $\text{W}/\text{cm}^2 \text{ nm}$ ) is combined with the factors described above to convert the data in units of  $[\text{A} \cdot \text{s}]$ . Subsequently, a series of conversion factors are applied to transform the data in units of counts. The conversion assumes that the 16-bit dynamic range is matched to the voltage dynamic range in the detector readout. According to the detector data sheet, the optimal available voltage range is approximately 2.2 V. Therefore, the total counts are calculated as:

$$\text{counts [DN]} = F_i \cdot A \cdot \text{efficiency} \cdot QE \cdot \Delta\lambda_\lambda \cdot t_{\text{exp}} \cdot \text{conversion factors}, \quad (13)$$

where  $F_i$  represents the flux of each data point in the input spectrum.

#### 4.4 Adding astrophysical and instrumental noise sources

The result from the previous step represents the net source signal, excluding all noise sources except for the zodiacal background, which we include in the target source signal. For realistic simulations, additional noise components such as photon noise, bias, and dark current must be considered.

Photon noise, which follows Poisson statistics, is modelled as the square root of the net signal in units of  $e^-$ . To simulate the distribution of photons striking the detector, we include a random component to the photon noise which is drawn from a Gaussian distribution with  $\mu=0$  and  $\sigma=\sqrt{\text{net signal}}[e^-]$ . Finally, to align the photon noise with the units of the source signal, photon noise is converted from  $e^-$  to counts.

Dark current was determined by empirically fitting a series of measurements taken at different temperatures, and it was found to scale according to the following relationship

$$I_d(T) = 105.94 \cdot e^{0.0684 \cdot T}, \quad (14)$$

where  $T$  is the temperature of the detector. Based on this equation,

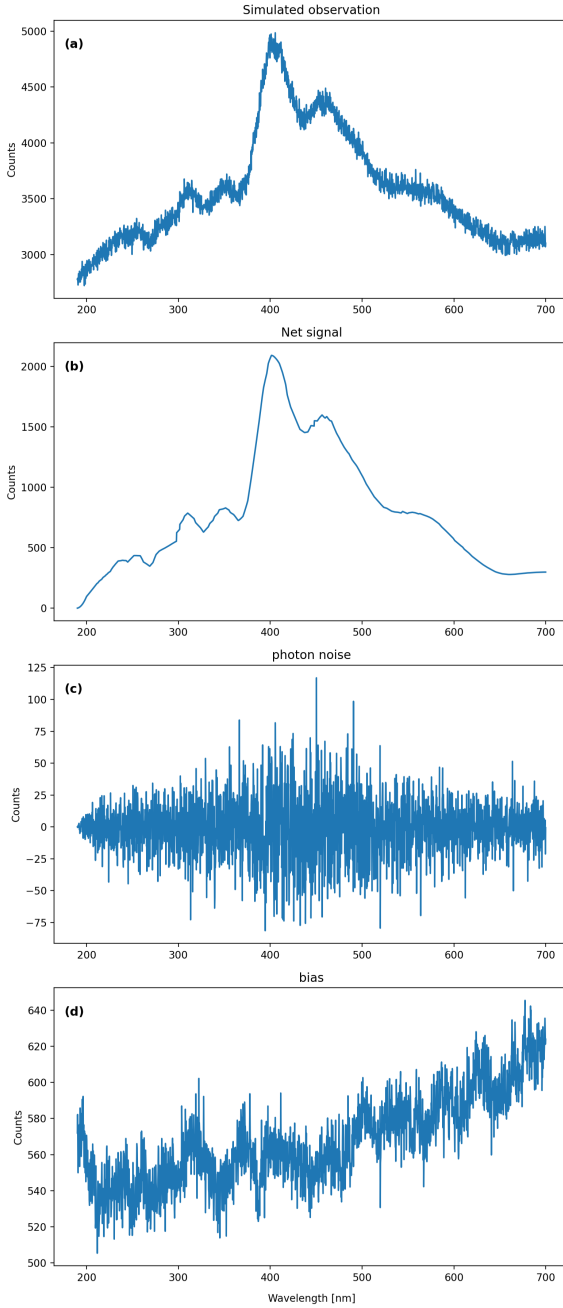


**Figure 7.** Simulation of HD 143459 using an exposure time of 5 s. The final simulated observation and its components are shown as well. Panel (a): output Mauve spectrum as simulated by the software. Panel (b): net simulated signal source. Panel (c): photon noise. Panel (d): bias noise.

the dark current is 445 counts/s at 21°C. This noise component is added by drawing random samples from a Poisson distribution with expectation value equal to  $I_d(T)$  multiplied by the exposure time.

In addition, the bias noise is included. The bias is an offset applied to the ADC (Analogue-to-Digital Converter) to prevent negative counts during readout. The bias was measured in the lab and found to have an average value of 600 counts per pixel across the detector (Fig. 7 (d)).

The output of the MauveSim's workflow is a 1D raw data spectrum similar to Fig. 7 (a). The simulator can also create a time series

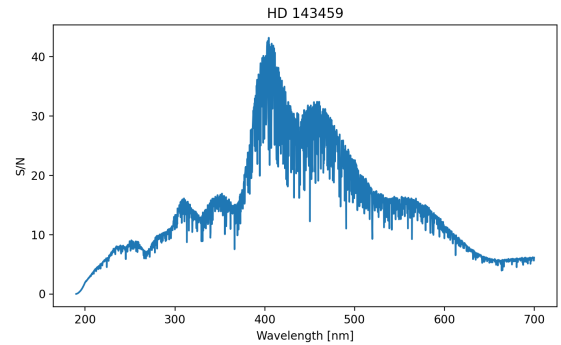


**Figure 8.** The S/N per pixel of the simulated data in Fig. 7.

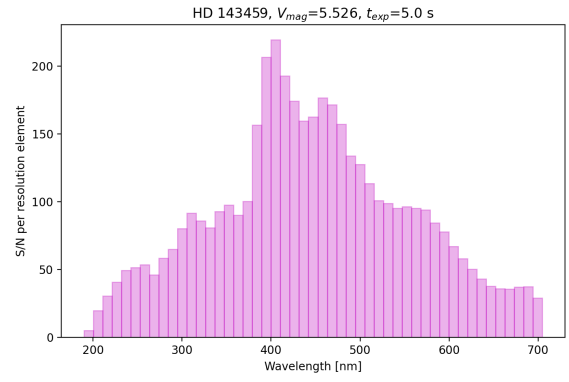


**Figure 9.** S/N per resolution element on the simulation of HD 143459 for a exposure time of 5 s.

observation, where multiple frames obtained with the same exposure time are stacked up together to simulate a longer observation.

#### 4.5 Signal-to-noise calculation

The S/N for each pixel, is calculated as follows

$$S/N|_{\text{pix}} = \frac{S}{\sqrt{\sigma_S^2 + \sigma_R^2 + \sigma_D^2}}, \quad (15)$$

where  $S$  is the net signal in units of counts (Fig. 7 (b));  $\sigma_S$  is the photon noise ( $\sqrt{S}$ );  $\sigma_R$  is the readout noise (equal to approximately 12 counts);  $\sigma_D$  is the dark current noise (equal to the sqrt of the dark current, i.e.  $\sqrt{\sim 2220}$  counts for the example in Fig. 7). Fig. 8 displays the S/N per pixel of HD 143459 for a 5 s integration.

Alternatively, the S/N can be calculated per resolution element (Fig. 9). This involves summing the signal from all pixels within the resolution element (10.5 nm, or approximately 40 pixels) linearly, while combining the corresponding noise components in quadrature:

$$S/N|_{\text{bin}} = \frac{\sum_i S_i}{\sqrt{\sum_i N_i^2}} \quad (16)$$

where  $i = \{k \mid \lambda_k \in [\lambda_{\text{lower}}, \lambda_{\text{upper}}]\}$ ,  $\lambda_{\text{lower}} = \lambda_{\text{current}}$ ,  $\lambda_{\text{upper}} = \lambda_{\text{lower}} + \Delta\lambda$ ,  $\Delta\lambda = 10.5$  nm.

## 5 SCIENCE CASE STUDIES

The “sweet spot” for Mauve’s science is spectrophotometric monitoring of bright stellar sources in the near UV and visible wavelengths (200–700 nm) to search for variability on timescales ranging from minutes to weeks and months.

Mauve’s performance allows it to effectively study flares in nearby active stars with observations not possible with any facility to date. For this reason, we will analyse this science case in detail, as it is Mauve’s “flagship science”. At the same time, other science areas can benefit from the same type of observations (spectrophotometric variability across the mid-near UV and visible bands). These include the study of variability in young, active stars such as Herbig Ae/Be stars, the study of variability in (more evolved) Be stars, monitoring of active binaries and characterisation of blue straggler stars.

### 5.1 Flaring solar-type stars

Our own Sun is a very quiet star compared to similar-type stars in the Galaxy. The advent of white light monitoring space telescopes dedicated to exoplanetary transit searches (e.g., Corot, Kepler, TESS) has shown that even in visible light many stars emit significant flares, much larger than anything observed in the Sun. However, during a flaring event, each wavelength probes a distinct region of the solar atmosphere. Consequently, while the white light curves provided by Kepler and TESS enable valuable statistical analyses of flare frequency across large stellar samples, they offer only limited potential for exploring the underlying physics of these events.

A broader wavelength coverage of flaring events achievable with Mauve can enable the different spectral components to be disentangled. While with e.g. Kepler and TESS data, one sees the tail of the emission in white light, observations with Mauve would allow to test models of the emission from the heated stellar photosphere and lower chromosphere; different models of this exist, which scientists are interested to compare against actual observations. In particular, flares observed in white light are probably the result of light emitted from the heated, optically thick photosphere and lower chromosphere, that are likely to reach temperatures of 10,000 K or so, peaking in the near-UV band. By observing only the white light, one effectively sees the peak of the iceberg, while missing the bulk of it. With its wide wavelength coverage and the capacity to monitor specific sources for long periods, Mauve is ideal for studying individual large flares in detail, advancing the understanding of their physical mechanisms. Many exoplanets have been detected around active stars, and the UV emission from the host star dramatically influences the planetary evolution. Understanding the nature of this UV emission is crucial to gaining insights into broader topics, such as habitability.

We know from Kepler and TESS data that some stars similar to the Sun undergo “super flares”, events in which their white light increases by several percent (events up to some 25% flux increase in the Kepler band have been observed, e.g. [Shibayama et al. \(2013\)](#) for the star KIC 12354328). If this flux rise is indeed produced by a heated patch of the photosphere, the increase in the blue and even more in the UV will be much larger, creating a “sweet spot” for Mauve observations. To demonstrate Mauve’s capabilities under different stellar brightness scenarios, we selected two example stars and used MauveSim to generate simulated observations. The example stars are a bright K2V star with  $V_{\text{mag}}=3.7$  and a G2V star with a visual magnitude of 7.4.

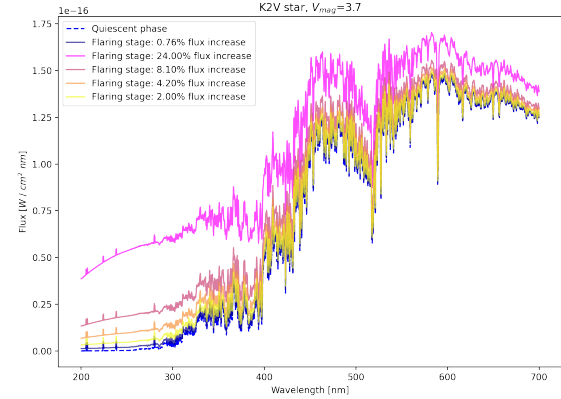


**Figure 10.** Example input spectra of a K2V star at different flaring stages. The quiescent spectrum is displayed in a dashed blue line. The flaring spectra contain a blackbody component with a temperature of 10,000 K that becomes increasingly more pronounced as the flare approaches its peak.

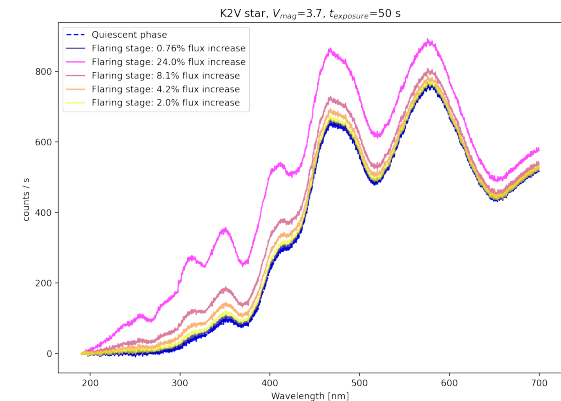


**Figure 11.** Simulated spectra of a K2V star at different flaring stages, as observed by Mauve. These spectra, generated with MauveSim, have been background-subtracted, i.e. the average noise floor has been removed from each data point and the data divided by the exposure time.

#### 5.1.1 K2V star

The input spectra used to simulate the flare on the K2V star are shown in Fig. 10. These display the stellar spectrum at different flaring stages, from the quiescent phase indicated with a dashed blue line, to the flare peak in magenta, and at varying decaying stages (the rest of the spectra in between). The flaring spectra include an additional component to them, which is a simplistic model of a blackbody at 10,000 K that becomes increasingly stronger as we approach the peak flaring stage. By selecting an integration time of 50 s, we simulated how Mauve would see such spectra assuming the current performance. The corresponding MauveSim simulated spectra are shown in Fig. 11. The low resolution of the instrument does not allow to retrieve individual lines. However, the quiescence, flare peak and decay stages are clearly distinguishable from one another. We can clearly see a high contrast among spectra across the wavelength range accessible to Mauve, and specifically in the UV.

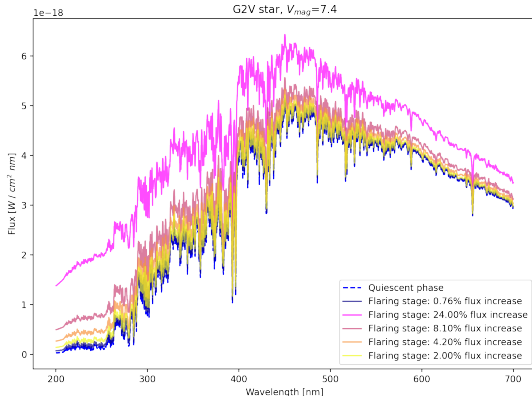


**Figure 12.** Example input spectra of a G2V star at different flaring stages. The quiescent spectrum is displayed in a dashed blue line. The flaring spectra contain a blackbody component with a temperature of 10,000 K that becomes increasingly more pronounced as the flare approaches its peak.

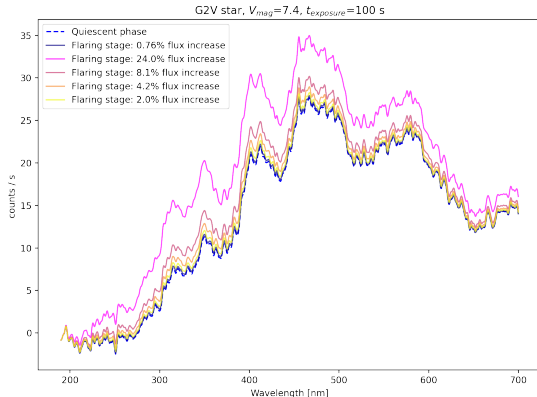


**Figure 13.** Simulated spectra of a G2V star at different flaring stages, as observed by Mauve. These spectra, generated with MauveSim, have been background-subtracted, i.e. the average noise floor has been removed from each data point and the data divided by the exposure time. Additionally, a Gaussian kernel with a FWHM of 10.5 nm was applied to the spectra to reduce noise and help distinguish the different flaring phases. This is an example near the limiting magnitude accessible to the Mauve’s flaring stars science case.

Separating the various flare phases will be paramount for scientists who will want to test models of flare physics in solar-type stars.

### 5.1.2 G2V star

For bright targets (V magnitude brighter than 6) Mauve can do excellent science on large flares, even in the presence of the high level of dark current which is its limiting factor. When going to fainter magnitudes, the dark current becomes the limiting factor, and, at magnitudes of 7.5 or so, even for a large flare such one with a 25% increase in the Kepler band, the noise level will limit the science that can be achieved. It is worth recalling that while in a photon noise limited regime (where the source flux is low but the background is lower) integrating for a long time allows to achieve higher signal to

noise observations (increasing with the square root of the observing time), in a background limited regime little if anything is gained through a long integration (as the background will also correspondingly increase).

Figure 13 provides an example that is considered to be near the limiting magnitude for Mauve’s flaring stars science case, i.e. the same large flare as for the K2V star, simulated for the fainter G2V stellar target in Fig. 12 ( $V_{\text{mag}} = 7.4$ ). While the spectrum at peak flare is clearly distinguishable from the quiescent phase, the noise level, in particular in the UV where the signal is low, is considerably high, so that it would be challenging to distinguish, e.g., different models for the flaring component.

## 6 CONCLUSIONS

At Blue Skies Space we developed MauveSim, an in-house instrument simulator to support the Mauve mission. This software generates simulated observations by requiring an input spectrum representative of the target source, which can either be an observed spectrum from other facilities or a synthetic model spectrum. The input spectrum is processed through the instrument response, incorporating its spectral resolution, optical element efficiencies, and detector response. Astrophysical and instrumental noise sources are then added to the net source signal. Users can specify the integration time, and the simulator produces a simulated raw spectrum as output. This tool is crucial in helping members of the Mauve science team refine their science cases and evaluate the feasibility of proposed observations. The software is accessible to all scientists who currently are or will be involved in the mission. Scientists not yet part of the Mauve survey are encouraged to explore the software by contacting BSSL by email at [info@bssl.space](mailto:info@bssl.space).

## ACKNOWLEDGEMENTS

The Mauve project has received funding from the European Union’s Horizon Europe research and innovation programme under grant agreement No. 101082738.

## DATA AVAILABILITY

Data utilised as input to perform the simulations are publicly available in the HST/STIS Stellar Library at <http://astro.wsu.edu/hststarlib/>.

## REFERENCES

- Archer, R., Tessenyi, M., Tinetti, G., Tennyson, J., Faulkes, M. C., Savini, G., Windred, P., Brown, D., Edwards, B., Stotesbury, I., Joshua, M., & Wilcock, B., 2020. A sustainable path for space science, *Nature Astronomy*, **4**, 1017–1018.
- Bradley, L., Stotesbury, I., Windred, P., & Tessenyi, M., in prep. The payload in the loop algorithm for mauve, *RASTI*, In preparation.
- Egan, A., France, K., Nell, N., DeCicco, N., Suresh, A., Kohnert, R., Fleming, B. T., & Ulrich, S., 2022. The colorado ultraviolet transit experiment: The first dedicated ultraviolet exoplanet mission.
- HAMAMATSU, 2024. *CMOS linear image sensors*, HAMAMATSU PHOTONICS K.K., Solid State Division, Accessed on October, 2024.
- Indahl, B., & Wilson, D., 2022. MANTIS: Monitoring Activity from Nearby sTars with uv Imaging and Spectroscopy, NASA Prop. ID 22-APRA22-121.

Leinert, C., Bowyer, S., Haikala, L. K., Hanner, M. S., Hauser, M. G., Levasseur-Regourd, A. C., Mann, I., Mattila, K., Reach, W. T., Schlosser, W., Staude, H. J., Toller, G. N., Weiland, J. L., Weinberg, J. L., & Witt, A. N., 1998. The 1997 reference of diffuse night sky brightness, *A&AS*, **127**, 1–99.

National Academies of Sciences Engineering, and Medicine, 2021. *Pathways to Discovery in Astronomy and Astrophysics for the 2020s*.

Pal, T., Khan, I., Worthey, G., Gregg, M. D., & Silva, D. R., 2023. HST Low-resolution Stellar Library, *ApJS*, **266**(2), 41.

Shibayama, T., Maehara, H., Notsu, S., Notsu, Y., Nagao, T., Honda, S., Ishii, T. T., Nogami, D., & Shibata, K., 2013. Superflares on Solar-type Stars Observed with Kepler. I. Statistical Properties of Superflares, *ApJS*, **209**(1), 5.

Stotesbury, I., Windred, P., & Tessenyi, M., in prep. Mauve technical note, In preparation.

This paper has been typeset from a  $\text{\TeX}/\text{\LaTeX}$  file prepared by the author.